Rev. Roum. Sci. Techn.– Électrotechn. et Énerg.
Vol. **71**, *1*, pp. 33–38, Bucarest, 2026

POWER LOSS ANALYSIS AND CONTROL OF A BIDIRECTIONAL HIGH-GAIN CONVERTER FOR EV CHARGING USING PV ARRAY

ANJANA ETHIRAJAN[1], RAMAPRABHA RAMABADRAN[2]

Keywords: Bidirectional converter; High gain; Photovoltaic (PV) array; Power loss analysis; Electric vehicle (EV) charging; Relay feedback; MATLAB.

This study looks at how a bidirectional high-gain converter (BDHGC) can support charging electric vehicles (EVs) using a PV array. The solar irradiation varies, and the PV system's output is increased with an MPPT technique before it is sent to the BDHGC. The converter increases the voltage and allows power to move back and forth for successful charging. Both switching and conduction losses are studied in detail by building MATLAB/Simulink simulations. The system uses a relay feedback control system to keep the output voltage steady whenever the load changes. From the simulation, it is evident that the system gives high efficiency and stable control, which makes voting solar-powered EV charging a possibility.

1. INTRODUCTION

Development towards sustainability is leading to increased use of electric vehicles in transportation. Given that EVs are helpful for the environment and rely less on fossil fuels, the need to develop a solid charging infrastructure becomes necessary. The DC-DC converter is a key component of this system because it helps move power between different voltages [1–3]. BDHGCs have proven to be a good fit for this work since they can operate in both charging and discharging modes [4–6]. They are most used when the electricity comes from a low-voltage source, such as a 60 V battery or solar panel, and it needs to be raised in voltage. This configuration makes it possible for the BDHGC to increase the voltage to 325 V so that EVs, V2G car drivers, and renewable-based systems can all use it.

The work focuses on a building with deck glazing and an integrated PV array, which is subject to variations in isolation. This process uses an MPPT technique so that the PV system gives off its optimal power before it gets sent to the converter [7–9]. Three switches, two inductors, and three capacitors make up the converter topology. Using MATLAB/Simulink, the circuit is tested to observe the dropping of power during switches and the increase in power when connections are made, when running on a 60 V input and keeping the output at 325 V steady. A simulation is run to find out how the converter changes at different frequencies, to find a suitable operating range [10,11]. To adjust the voltage output according to load, both relay and PI control are combined. This type of feedback uses changes in voltage to respond swiftly to any changes. On the other hand, the PI controller tackles steady-state errors and guarantees that the output voltage is steady. Having all these techniques in place enables the system to manage voltage quickly and accurately [12].

Following that, the paper proposes the converter's physical layout, carefully examines the losses involved, designs the control systems, and gives results from simulations to show that this method is useful for charging electric vehicles with renewable energy. Fig. 1 depicts the architecture of the PV with BDHGC for EV charging.

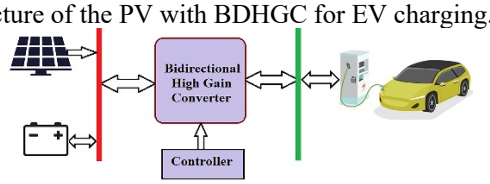

Fig. 1 – Architecture of PV with BDHGC for EV charging.

The structure of this paper is outlined as follows. Section 2 covers the modeling of the photovoltaic (PV) system, considering the impact of changing solar irradiance. Section 3 introduces the architecture and working mechanism of the Bidirectional High-Gain Converter (BDHGC). In Section 4, the focus shifts to a comprehensive evaluation of power losses, specifically addressing both switching and conduction losses. Section 5 discusses the implementation of the control methodology used to maintain output voltage stability, which integrates relay feedback and proportional-integral (PI) control techniques. Section 6 highlights the simulation results carried out in MATLAB/Simulink, demonstrating the system's performance under various conditions. Finally, Section 7 concludes the paper with a summary of the main outcomes and insights into the potential of the proposed setup for use in renewable energy-driven EV charging applications.

2. MODELLING OF PV

The PV array is modelled at 30 V and 3.3 kW. Here, a 37 W panel is connected to 2×45 to obtain 3.3 kW under standard test conditions (STC). To accurately describe the electrical properties of PV, the single-diode equivalent model is used. This model covers a current source that relies on light, a diode, and resistance to represent losses within the device. The current output of a PV array depends on the terminal voltage and is affected by temperature and sunlight. The equivalent circuit model with design equation is discussed in [7]. The parameters of the 3.3 kW PV array are depicted in Table 1.

Table 1

Parameter for PV Array at 3.3 kW.

Parameters	Values
Power at MPP	3.33 kW
Voltage at MPP	33.12 V
Current at MPP	101.25 A
Open circuit voltage	42.48 V
Short circuit current	114.75 A
No. of panel in series and parallel	2×45

In this study, the PV array is tested under varying levels of solar isolation to observe the system's response to changes in energy availability. These variations directly affect the PV output and are critical in evaluating the dynamic performance of the converter and control strategy. The simulated characteristics of the PV array at different insolation (G) with the same temperature (T) are obtained as shown in Fig. 2. Table 2 tabulates the values of voltage (V_{pv}), current, and power of the PV array with different insolation.

[1,2]Department of Electrical and Electronics Engineering, Sri Sivasubramaniya Nadar College of Engineering, Kalavakkam-603110, Tamilnadu, India. E-mails: anjanae@ssn.edu.in, ramaprabhar@ssn.edu.in

DOI: 10.59277/RRST-EE.2026.1.6

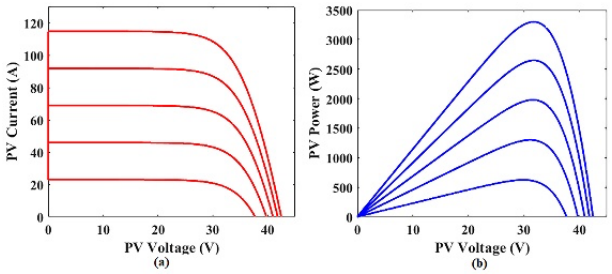

Fig. 2 – Characteristics of PV array with different insolation (a) PV voltage vs PV current (b) PV voltage vs PV power.

Table 2

PV voltage, current, and power at different irradiation.

G (W/m^2)	T (°C)	V_{pv} (V)	I_{pv} (A)	P_{pv} (W)
1000	25	31.8	103.76	3299.6
800	25	31.8	83.23	2646.9
600	25	31.64	62.54	1978.74
400	25	31.16	41.73	1300.35
200	25	29.91	20.83	623

Since the direct output from the PV array is not consistent and its voltage fluctuates, a special boost converter increases it from 30 V to 60 V. It also implements a Maximum Power Point Tracking (MPPT) (P&O) algorithm to guarantee the most efficient energy use [7], [9]. This voltage is then applied to the Bidirectional High-Gain DC-DC Converter (BDHGC), which takes over handling further voltage increases and control in both directions.

3. OVERVIEW OF CONVERTER TOPOLOGY

The converter topology of BDHGC contains three active switches, S_1, S_2, and S_3, connected to two inductors, L_1 and L_2, along with three capacitors, C_1, C_2, and C_3. The developed configuration reaches high voltage boost performance while maintaining controlled switch voltage levels, which aligns perfectly with EV charging requirements that require a small size along with power efficiency and bidirectional energy management capabilities. The circuit diagram of BDHGC is depicted in Fig. 3.

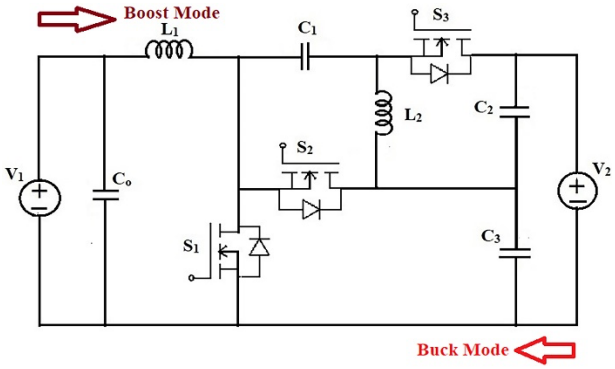

Fig. 3 – Circuit diagram of BDHGC [10,11].

A step-up process in this design boosts the low input voltage from the DC source (60V) to reach an output voltage level of 230V by interchanging energy between capacitors and inductors. The operation executes energy storage within inductors prior to controlled S_1, S_2, and S_3 switch operations that deliver stored energy to the load. The function of capacitors C_1 and C_2 includes performing voltage boosting functions while managing current ripple. The purpose of C_3 is to filter the output voltage for steady load performance.

Step-down (buck) mode enables the process of extracting an output voltage reduction from the high voltage load side by controlling the same switching components with passive elements in sequence. The bidirectional behavior of the converter permits both charging of EV batteries and grid support during regenerative braking and energy recovery procedures.

Detailed modes of operation have been explained in [10-11]. From that detailed study, the voltage gains for both boost (G_{bo}) and buck (G_{bu}) of the BDHGC are,

$$G_{bo}=\frac{1+D_{bo}}{1-D_{bo}} \tag{1}$$

$$G_{bu}=\frac{D_{bu}}{2-D_{bu}} \tag{2}$$

where, D_{bo} & D_{bu} are the duty cycle of boost and buck operation of BDHGC. The design equations for the parameters of the inductor and the capacitor are tabulated in Table 3.

Table 3

Design equations for inductor and capacitor values [1,2]

Parameters	Boost Mode	Buck Mode
Inductor Currents (RMS)	$I_{L1}=\frac{1+D_{bo}}{1-D_{bo}}I_o$ $I_{L2}=I_o$	$I_{L1}=I_{in}$ $I_{L2}=\frac{D_{bu}}{2-D_{bu}}I_{in}$
Inductor Values	$L_1=\frac{V_{bu}\times D_{bo}}{\Delta I_{L1}\times f_s}$ $L_2=\frac{V_{bu}\times D_{bo}}{\Delta I_{L2}\times (1-D_{bo})\times f_s}$	$L_1=\frac{V_{bo}\times (1-D_{bo})}{\Delta I_{L1}\times f_s}$ $L_2=\frac{V_{bo}\times (1-D_{bo})}{\Delta I_{L2}\times f_s}$
Capacitor Voltages	$V_{C1}=\frac{V_{bu}}{1-D_{bo}}$ $V_{C2}=\frac{V_{bu}\times D_{bo}}{1-D_{bo}}$ $V_{C3}=\frac{V_{bu}}{1-D_{bo}}$	$V_{C1}=V_{bo}$ $V_{C2}=\frac{V_{bo}}{2-D_{bu}}$ $V_{C3}=\frac{(1-D_{bo})\times V_{bo}}{D_{bu}}$
Capacitor Values	$C_1=\frac{I_{L2}\times D_{bo}}{\Delta V_{C1}\times f_s}$ $C_2=C_3=\frac{I_o\times D_{bo}}{\Delta V_{C2}\times f_s}$	$C_1=\frac{I_{L1}\times (1-D_{bo})}{\Delta V_{C1}\times f_s}$ $C_2=C_3$ $=\frac{I_o\times (1-D_{bo})}{\Delta V_{C2}\times f_s}$

The stability of the converter also performed and explained elaborately in [10]. The obtained transfer function for both the operations is given below,

$$T.F_{(bo)}=\frac{9.277\times 10^7 s^3-0.002031s^2-2.707\times 10^{17}s+1.679\times 10^4}{(s^5+325s^4-2.821\times 10^9 s^3-9.169\times 10^{11}s^2-1.164\times 10^{17}s-3.783\times 10^{19})} \tag{3}$$

$$T.F_{(bu)}=\frac{47102850000000+574425000000s}{(s^5+1435115s^3+1139429430s^2+178071750000s+14601883500000)} \tag{4}$$

The converter topology balances performance and complexity effectively to provide a suitable solution for EV charging stations needing high efficiency and bidirectional operation coupled with high voltage conversion ratios. The subsequent sections present discussions about power loss modeling and control methods for this conversion topology.

4. POWER LOSS ANALYSIS

Power loss accuracy stands as an essential factor during the design of high-efficiency converters. All power losses in the BDHGC topology align into three categories, including wire losses in switches and inductors, transitions in MOSFETs, and passive components' energy dissipation (ESR). Standard analytical models alongside datasheet data from devices enable the quantification of individual loss elements in this section of analysis. Figure 4 depicts the equivalent circuit diagram of the topology with parasitic components.

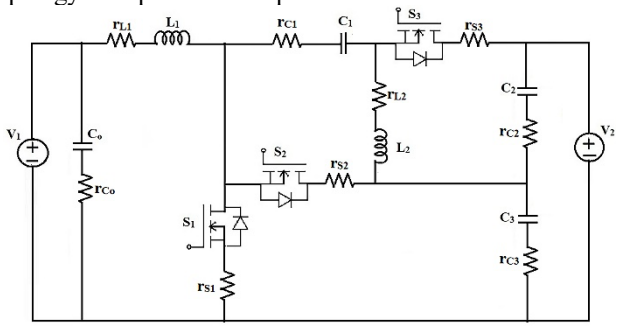

Fig. 4 – Equivalent circuit diagram of BDHGC with parasitic components.

The total power loss in the BDHGC arises from several key components, each contributing to reduced efficiency. Here's a comprehensive breakdown of the loss mechanisms.

4.1 INDUCTOR POWER LOSS

The equivalent series resistance (ESR) on inductors causes copper losses which vary according to the RMS current squared.

- Inductor Current (I_{L1})

The conduction loss (P_{L1}) is given by,

$$P_{L1}=I_{L1}^2 \times r_{L1}. \tag{5}$$

The RMS inductor current as given in Table 3 (considering boost mode) can be substituted in conduction losses.

For boost operation

$$P_{L1}=\left[\frac{1+D_{bo}}{1-D_{bo}} \times \frac{V_o}{R}\right]^2 \times r_{L1}. \tag{6}$$

For buck operation

$$P_{L1}={I_{in}}^2 \times r_{L1}. \tag{7}$$

- Inductor Current (I_{L2})

The conduction loss (P_{L2}) is given by,

$$P_{L2}=I_{L2}^2 \times r_{L2} \tag{8}$$

The RMS inductor current as given in Table 3 (considering boost mode) can be substituted in conduction losses.

For boost operation

$$P_{L2}=\left[\frac{V_o}{R}\right]^2 \times r_{L2}. \tag{9}$$

For buck operation

$$P_{L2}=\left[\frac{D_{bu}}{2-D_{bu}} \times I_{in}\right]^2 \times r_{L2}. \tag{10}$$

4.2 CAPACITOR POWER LOSS

The power dissipation through ESR takes place during both charging and discharging operations of capacitors. From all capacitors utilized, the one placed along the high-current path generates the greatest power loss because it encounters superior current density, while all other capacitors maintain relatively low currents. Each voltage ripple impact determines the amount of loss experienced by capacitors.

- Capacitor Voltage (V_{C1})

The RMS capacitor current from KCL [2] can be given by,

$$I_{C1} = I_{L2} - I_{L1}. \tag{11}$$

The values of I_{L2} and I_{L1} of as given in Table 3 (considering boost mode) can be substituted in conduction losses.

$$P_{C1}=I_{C1}^2 \times r_{C1}. \tag{12}$$

The values of I_{L2} and I_{L1} of as given in Table 3 (considering boost mode) can be substituted in conduction losses.

For boost operation

$$P_{C1}=\left(\frac{4{D_{bo}}^2}{(1-D_{bo})^2}\right)\left(\frac{V_o}{R}\right)^2 \times r_{C1}. \tag{13}$$

For buck operation

$$P_{C1}=\left(\left(\frac{D_{bu}}{2-D_{bu}}-1\right) \times I_{in}\right)^2 \times r_{C1}. \tag{14}$$

- Capacitor Voltage (V_{C2})

The RMS capacitor current from detailed study in [2] can be given by,

For boost operation

$$I_{C2} = \frac{I_o}{2}\sqrt{1-D_{bo}}. \tag{15}$$

For buck operation

$$I_{C2} = \frac{I_o}{2}\sqrt{1-\frac{D_{bu}}{2-D_{bu}}}. \tag{16}$$

The conduction loss for V_{C2} is given by,

$$P_{C2}=I_{C2}^2 \times r_{C2} \tag{17}$$

The values of I_{L2} and I_{L1} of as given in Table 3 (considering boost mode) can be substituted in conduction losses.

For boost operation

$$P_{C2}=\left(\frac{V_o}{4R}\right)^2 \times (1-D_{bo}) \times r_{C2}. \tag{18}$$

For buck operation

$$P_{C2}=\left(\frac{V_o}{4R}\right)^2 \times \left(1-\frac{D_{bu}}{2-D_{bu}}\right) \times r_{C2}. \tag{19}$$

- Capacitor Voltage (V_{C3})

The RMS capacitor current from detailed study in [2] can be given by,

For boost operation

$$I_{C3} = I_o\sqrt{1-D_{bo}}. \tag{20}$$

For buck operation

$$I_{C3} = I_o\sqrt{1-\frac{D_{bu}}{2-D_{bu}}}. \tag{21}$$

The conduction loss for V_{C3} is given by,

$$P_{C3}=I_{C3}^2 \times r_{C3} \tag{22}$$

The values of I_{L2} and I_{L1} of as given in Table 3 (considering boost mode) can be substituted in conduction losses.

For boost operation

$$P_{C3}=\left(\frac{V_o}{R}\right)^2 \times (1-D_{bo}) \times r_{C3}. \tag{23}$$

For buck operation

$$P_{C3}=\left(\frac{V_o}{R}\right)^2 \times \left(1-\frac{D_{bu}}{2-D_{bu}}\right) \times r_{C3}. \tag{24}$$

4.3 SWITCHING POWER LOSS

Each MOSFET loses power because of its on-state resistance, which occurs during current conduction. The main switch responsible for bearing higher current flow generates

most of this heat loss. The contribution of auxiliary switches leads to minor but relevant power losses.

- Switch (S_1)

For boost operation

The conduction loss for S_1 is given by,

$$P_{cond,S1}=I_{L1}^2 \times R_{ds(ON)} \times D_{b0}. \quad (25)$$

The values of I_{L1} of as given in Table 3 (considering boost mode) can be substituted in conduction losses.

$$P_{cond,S1}=\left[\frac{1+D_{bo}}{1-D_{bo}} \times \frac{V_o}{R}\right]^2 \times R_{ds(ON)} \times D_{b0}. \quad (26)$$

The switching loss for S_1 is given by,

$$P_{sw,S1}=\frac{1}{2} \times V_{C1} \times I_{L1} \times (t_r + t_f) \times f_s. \quad (27)$$

The values of V_{C1} and I_{L1} of as given in Table 3 (considering boost mode) can be substituted in switching losses.

$$P_{sw,S1}=\frac{V_o^2}{2(1-D_{bo})R} \times (t_r + t_f) \times f_s. \quad (28)$$

For buck operation

The conduction loss for S_1 is given by,

$$P_{cond,S1}=I_{in}^2 \times R_{ds(ON)} \times (1 - D_{bu}). \quad (29)$$

The switching loss for S_1 is given by,

$$P_{sw,S1}=\frac{1}{2} \times V_{bo} \times I_{in} \times (t_r + t_f) \times f_s. \quad (30)$$

- Switch (S_2 & S_3)

The conduction loss for per switch is given by,

$$P_{cond,S2/S3}=I_{L2}^2 \times R_{ds(ON)} \times (1 - D_{b0}). \quad (31)$$

The values of I_{L1} of as given in Table 3 (considering boost mode) can be substituted in conduction losses.

$$P_{cond,S2/S3}=\left[\frac{D_{bu}}{2-D_{bu}} \times I_{in}\right]^2 \times R_{ds(ON)} \times D_{bu}. \quad (32)$$

The switching loss for per switch is given by,

$$P_{sw,S2/S3}=\frac{1}{2}\frac{(1 - D_{bu})V_{bo}}{D_{bu}} \times \frac{D_{bu}\, I_{in}}{2 - D_{bu}} \times (t_r + t_f) f_s \quad (33)$$

4.4 TOTAL POWER LOSS AND EFFICIENCY

The total power loss is the sum of all three losses for both boost and buck operation. The equation is given below,

$$P_{total}=P_{L1} + P_{L2} + P_{C1} + P_{C2} + P_{C3} + P_{cond,S1} + P_{sw,S1} + 2(P_{cond,\frac{S2}{S3}} + P_{sw,\frac{S2}{S3}}). \quad (34)$$

By considering all losses in each component, the efficiency is calculated as,

$$\eta=\frac{P_o}{(P_o+P_{total})}. \quad (35)$$

5. CONTROL TECHNIQUE FOR BDHGC

A control strategy using relay feedback together with a proportional-integral (PI) controller ensures stable voltage regulation across different operating conditions for the BDHGC as shown in Fig. 5. The hybrid control strategy activates relay feedback together with a PI controller to achieve high dynamic response speed from relays and maintain precise performance in EV charging applications.

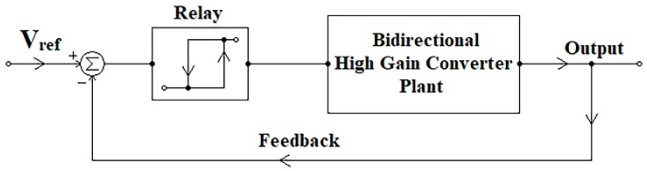

Fig. 5 – Block diagram of BDHGC with relay feedback.

Relay feedback control utilizes the principle of hysteresis control. The converter output voltage receives continuous monitoring along with reference voltage assessment to establish a predefined voltage threshold. The converter output voltage undergoes switching when it deviates from specific threshold zones. When the relay state changes between ON and OFF positions it controls the converter's switching behavior [12].

The binary control action enables the system to swiftly react to brief voltage fluctuations that occur due to changes in load or disturbances in the input. The control signal *u(t)* for a simple relay controller is defined as:

$$u(t)=\begin{cases}+U, if\ V_o < V_{ref} - \Delta, \\ -U, if\ V_o > V_{ref} + \Delta.\end{cases} \quad (36)$$

A tolerance zone represented by the symbol Δ surrounds the reference voltage to stop continuous switching. The relay output $u(t)$ operates the switches through gate signals to preserve the output voltage within a tight bandwidth.

Also relay feedback control receives additional stabilization through the implementation of a PI controller. A control signal emerges directly from the PI controller through processing the error signal. The PI controller computes a control signal $u_{P1(t)}$ based on the error signal $e(t)=V_{ref}-V_o$

$$u_{P1(t)}=K_p\,.\,e(t) + K_i \int e(t)\mathrm{d}t. \quad (37)$$

In the proportional term, the output immediately reacts to reference or load variations, whereas the integral action eliminates steady-state errors through time-based integration of voltage deviations. The controller combines a relay for transient response speed and a PI for eliminating steady-state error. The system design combines PI controller continuous modulation outputs with relay controller fast gating signals in transient operation. The system determines controller usage through a switching logic by comparing deviation values to set thresholds.

6. SIMULATION RESULTS

A comprehensive Simulink model of the BDHGC demonstrated its functionality from boost mode (60 V to 325 V) through buck mode (325 V to 60 V) at 25 kHz switching frequency [13]. The converter achieves precise steady-state voltage regulation alongside fast transient response through its hybrid control method of relay feedback with proportional-integral control.

The simulated model of BDHGC with controller is depicted in Fig. 6. The input and output waveform of voltage, current, and power for BDHGC are shown in Fig. 7 and 8. The voltage stress across switches S_1 to $S_{3\ is}$ depicted in Fig. 9 and10 for BDHGC.

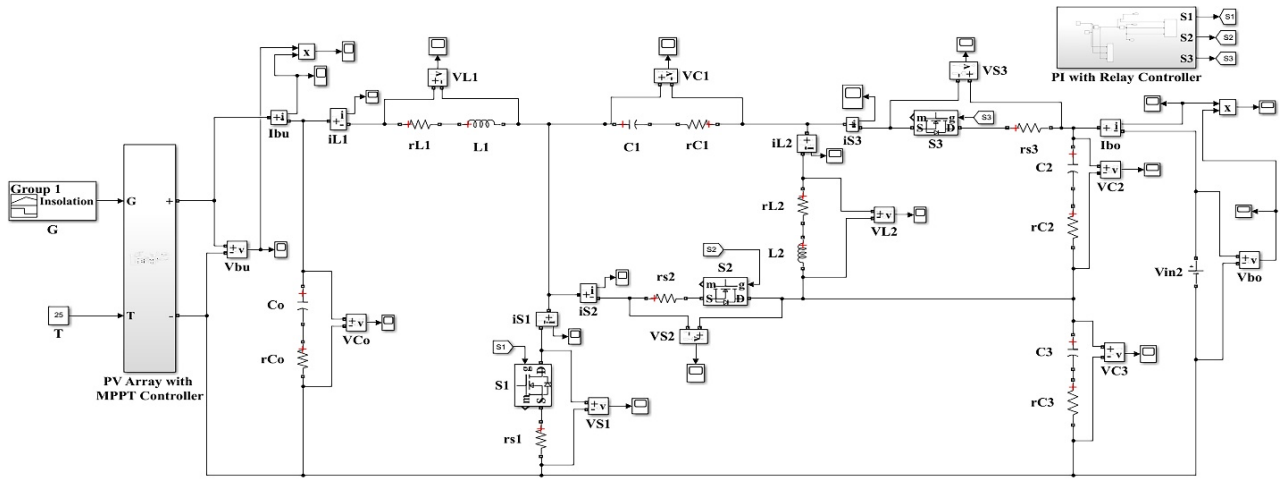

Fig. 6 –Equivalent series Simulink model of BDHGC with controller.

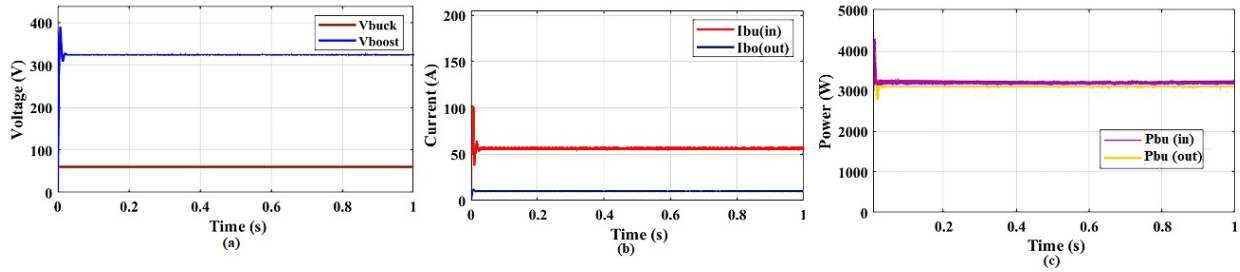

Fig. 7 – Input and output results for boost operation (a) voltage (b) current (c) power.

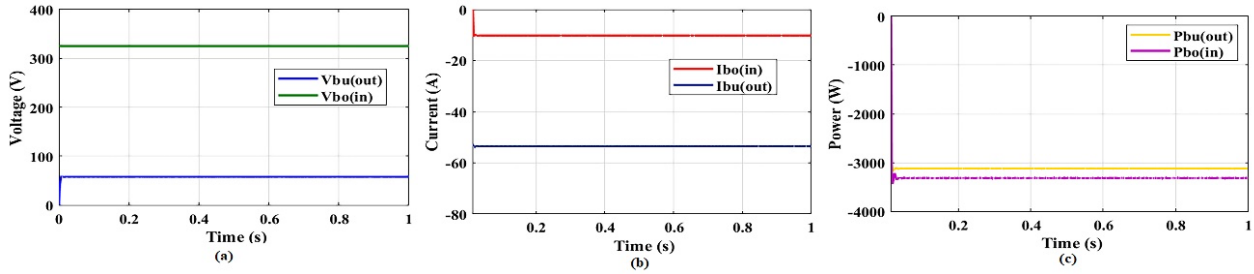

Fig. 8 – Input and output results for buck operation (a) voltage (b) current (c) power.

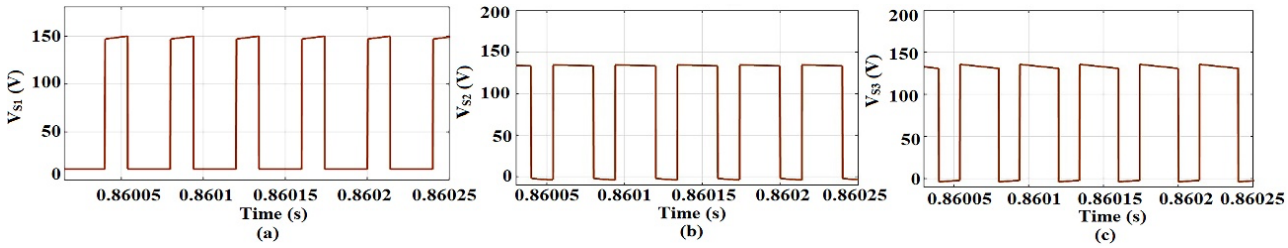

Fig. 9 – Voltage stress for boost operation (a) switch 1 (b) switch 2 (c) switch 3.

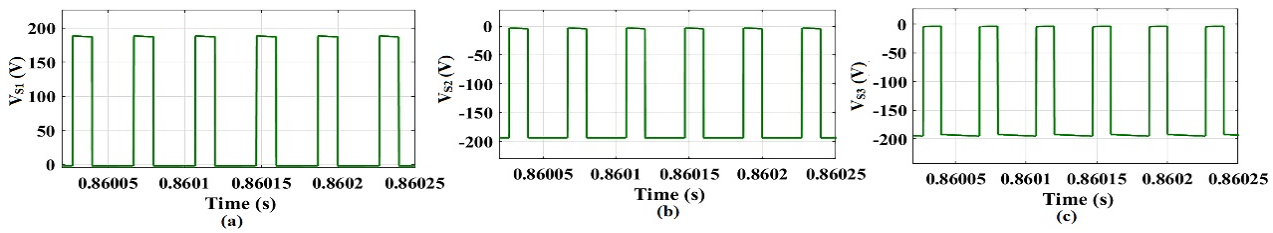

Fig. 10 – Voltage stress for buck operation (a) switch 1 (b) switch 2 (c) switch 3.

The results obtained for BDHGC in both boost and buck operation are tabulated in Table 4.

Table 4

Simulation results for both the operation

Parameters	Operations	
	Boost	Buck
Input, Output Voltage	60 V, 321 V	325 V, 58.8 V
Input, Output Current	54.9 A, 10.03 A	-10.13 A, -54.1 A
Input, Output Power	3294 W, 3220 W	-3292 W, -3181 W
Efficiency	97.7 %	96.6%
Inductor Currents (I_{L1}, I_{L2})	54.7 A, -10.03 A	-10.13 A, 53.9 A
Capacitor Voltage (V_{C1}, V_{C2}, V_{C3})	140 V, 131 V, 190 V	135 V, 130 V, 195 V
Settling Time (ms)	~95	~80

The total power loss in the BDHGCI converter is the sum of losses from inductors, capacitors, and semiconductor switches (MOSFETs). Based on the datasheet values of Infineon-IRFP250N: $R_{ds(on)}$ = 75 mΩ, t_r = 43 ns, t_f = 33 ns. Fig. 11 represents the graphical structure of the comparative power loss distribution for BDHGC. From the graphical representation of comparative power loss distribution as shown in Fig. 11, the total power loss attained for boost operation is 55.5 W, and for buck operation is 108.9 W.

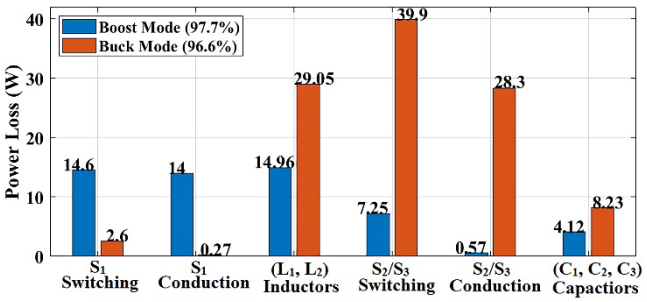

Fig. 11 – Graphical representation of comparative power loss distribution for BDHGC.

7. CONCLUSIONS

This study examines the power loss characteristics and control methods of a bidirectional high-gain converter (BDHGC) connected to a photovoltaic (PV) array for electric vehicle (EV) charging applications. The PV array delivers power under varying sunlight conditions, which the converter boosts to the required voltage for EV charging. Simulations demonstrate that the relay feedback control effectively maintains a stable output voltage. A detailed analysis of switching and conduction losses confirms that the converter operates efficiently within anticipated parameters. These results highlight the BDHGC's suitability for renewable energy-powered EV charging systems, offering dependable and efficient performance.

ACKNOWLEDG(E)MENT(S)

The author sincerely thanks the supervisor for their invaluable guidance and the institution for its continuous support throughout this research.

CREDIT AUTHORSHIP CONTRIBUTION STATEMENT

Anjana Ethirajan: investigation, validation, draft writing
Ramaprabha Ramabadran: methodology, resources, writing, review, and editing

Received on 6 June 2025

REFERENCES

1. M.C. Annamalai, N.A. Prabha, *A comprehensive review on isolated and non-isolated converter configuration and fast charging technology: for battery and plug in hybrid electric vehicle*, Heliyon, **9**, *8* (2023).
2. L. Yu, L. Wang, C. Yang, L. Zhu, Y. Gan, H. Zhang, *A novel nonisolated gan-based bidirectional dc–dc converter with high voltage gain*, IEEE Transactions on Industrial Electronics, **69**, *9*, pp. 9052–9063 (2022).
3. S. Sangeetha, R. Ramaprabha, *Enhanced stability investigation of high-gain boost converter for photovoltaic system*, Rev. Roum. Sci. Techn. – Électrotechn. et Énerg., **70**, *4*, pp. 549–554 (2025).
4. V. Viswanatha, A.C. Ramachandra, R. Venkata Siva Reddy, *Bidirectional DC-DC converter circuits and smart control algorithms: a review*, Journal of Electrical Systems and Information Technology, **9**, pp. 1–29 (2022).
5. S. Lakshmi, R. Ramaprabha, *Stability evaluation of four-phase high-gain converter by small signal modeling*, Rev. Roum. Sci. Techn. – Électrotechn. et Énerg., **65**, pp. 75–80 (2020).
6. T-I. Voicila, G-C. Seritan, B-A. Enache, *Analysis of bidirectional dc-dc power converters for screening systems of retired batteries*, Rev. Roum. Sci. Techn. – Électrotechn. et Énerg., **69**, *3*, pp. 311–316 (2024).
7. M.S. Ulaganathan, R. Muniraj, R. Vijayanand, D. Devaraj, *Novel solar photovoltaic emulation for validating the maximum power point algorithm and power converter*, Rev. Roum. Sci. Techn. – Électrotechn. et Énerg., **68**, *4*, pp. 407–412 (2023).
8. R. Ramaprabha, E. Anjana, G. Balaji, N. Abhishek, R. Aswinkumar, *Investigation on the role of super capacitors in standalone PV system*, In IEEE Xplore, 2022 IEEE 2nd International Symposium on Sustainable Energy, Signal Processing and Cyber Security (iSSSC), Gunupur, Odisha, India, pp. 1–5 (2022).
9. S. Seba, M. Birane, K. Benmouiza, *A comparative analysis of boost converter topologies for photovoltaic systems using MPPT (PO) and beta methods under partial shading*, Rev. Roum. Sci. Techn. – Électrotechn. et Énerg., **68**, *4*, pp. 375–380 (2023).
10. P. Rajan, S. Jeevananthan, *An adjustable gain three-port converter for battery and grid integration in remote location microgrid systems*, Renewable Energy, **179**, pp. 1404–1423 (2021).
11. E. Anjana, R. Ramaprabha, *Extended analysis of non-isolated bidirectional high gain converter*, Advances in Electrical and Computer Engineering, **23**, *4*, pp. 89–98 (2023).
12. E. Anjana, R. Ramaprabha, *Mathematical modeling of buck converter with relay feedback*, Journal of Circuits, Systems, and Computers, **31**, *11* (2022).
13. *** www.mathworks.com